Ground-state properties of isolated interstitial iron in silicon: Electronic structure and hyperfine interactions

H. Weihrich and H. Overhof
Fachbereich Physik, Universität-GH Paderborn, D-33095 Paderborn, Federal Republic of Germany
(Received 28 February 1996)

We have performed *ab initio* total energy calculations for interstitial iron in silicon with particular emphasis on the matrix elements for the hyperfine interactions with the iron nucleus and with several silicon ligand nuclei. The total energy calculations have been performed in the general framework of the density functional theory (DFT) treating many-particle effects in the local spin-density approximation (LSDA). We use a Dyson's equation approach to solve the Kohn-Sham equation of the density functional theory and calculate the Green's function with the help of the linear muffin-tin orbital theory using the atomic-spheres approximation (ASA). Unfortunately the use of the ASA prohibits the inclusion of lattice relaxation effects. Our total energy calculations lead to a model for the electronic structure which is dominated by covalent hybridization of iron *d* states with silicon *p* states. From the results of our calculations we can easily explain the reaction of the electronic system when passing from Fe_i^0 to Fe_i^+. To this aim we slightly modify the Ludwig-Woodbury model: In a first step we consider the exchange splitting of the iron *d* states which in a second step are further split by the crystal field. The hyperfine matrix elements for $Si:Fe_i^0$ are calculated directly from the magnetization density obtained by the LSDA-DFT calculation and show excellent agreement with data from electron nucleus double resonance (ENDOR) experiments. For $Si:Fe_i^+$ we have to take into account the spin-orbit interaction of the iron *d* orbitals. Since our total energy calculations neglect spin-orbit interactions, we switch to a description which uses symmetry-adapted many-particle wave functions. With these functions we calculate the matrix elements for the hyperfine interaction with the iron nucleus and with several silicon ligand nuclei. We use the localization properties of our magnetization density to determine the many-particle wave function and to obtain data for the hyperfine interactions. We show that the covalent hybridization of the iron *d* states with iron *p* states and with silicon orbitals alone cannot explain the discrepancy between calculated and measured data for the hyperfine interaction with the iron nucleus. However, the additional consideration of a dynamical Jahn-Teller effect as a Ham effect leads to consistent data. The calculated data for the ligand hyperfine interaction allow one to definitely assign ligand shells to the measured ENDOR data. [S0163-1829(96)04431-1]

I. INTRODUCTION

During the last 30 years considerable work has been spent in order to understand the properties of transition-metal (TM) ions in semiconductors. Because it is practically omnipresent a special focus has been on iron in silicon, which has thereby become one of the best studied TM defects in semiconductors. The development started in the early 1960s with the famous work of Ludwig and Woodbury,[1] who investigated doped semiconductors by magnetic resonance experiments. In the following years experimental and theoretical work dealt with topics such as solubility,[2] electrical activity,[3,4] and also with ground-state properties studied by electron paramagnetic resonance (EPR),[1,5] electron nucleus double resonance (ENDOR),[6–10] and Mössbauer[11] spectroscopy. Due to the high mobility and reactivity of interstitial iron much attention was given to pair defects and aggregates containing iron (see, e.g., Ref. 12, and references therein).

The apparent puzzling duality of TM ions that some properties are understood in a covalent delocalized picture while other properties call for an atomically localized picture for the defects stimulated the first theoretical calculations on TM impurities in semiconductors.[13] The theoretical investigations were renewed in the 1980s with the development of the density functional theory (DFT),[14–18] which soon was applied to the problem of deep TM defects in semiconductors.[19–29] With the exception of the ''early interstitials'' and ''late substitutionals''[26] all theoretical work corroborated the main features of the model Ludwig and Woodbury[1] developed to describe their EPR results. Although many experiments have been performed to measure hyperfine interactions (hfi), only a few attempts have been made to calculate the hfi and these have been restricted to the neutral charge state $Si:Fe_i^0$ only.[11,23,28] To the best of our knowledge up to now no attempt has been made to calculate the hfi for the positive charge state $Si:Fe_i^+$. This may be due to the fact that the ground-state term of $Si:Fe_i^+$ is the orbital triplet $^4T_1$, the degeneracy of which is lifted by the spin-orbit interaction.

There is a controversial discussion as to the origin of the large reduction of the orbital angular momentum factor $g_{\tilde{l}}$ of the g factor of the ground state $g=\frac{5}{3}g_s-\frac{2}{3}g_{\tilde{l}}$ measured in EPR. This reduction has been interpreted in the literature assuming that $Si:Fe_i^+$ is a Jahn-Teller (JT) system showing a Ham effect.[30] Alternatively the reduction is explained by covalent hybridization. Katayama-Yoshida and Zunger[23] have shown that according to their calculations covalent hybridization is the dominant effect for the ground state. However, recent experiments[31–33] on optical transitions for $Si:Fe_i$ indicate that a dynamical JT effect may be present for the ''ex-

cited'' spin-orbit split states of the ground-state term $^4T_1$. We show based on calculated hfi matrix elements that covalent effects alone cannot explain the large reduction factor of the orbital angular momentum matrix elements for Fe_i^+. We therefore propose that the experimentally observed ground-state properties of Si:Fe_i^+ are due to covalent hybridizations and a dynamical JT effect.

Our paper is organized as follows: in Sec. II we sketch the general framework of our total energy calculations and summarize our results for Si:Fe_i^0 and Si:Fe_i^+ by means of a covalent model. Our calculations of hfi matrix elements are presented in Sec. III. Details of the calculations for Si:Fe_i^+ are given in the Appendix.

II. TOTAL ENERGY CALCULATIONS

A. Theoretical method

We have performed *ab initio* total energy calculations using the DFT (Refs. 14 and 15) in the local spin-density approximation[16–18] (DFT-LSDA) to determine the electronic ground state of deep impurities in silicon. Since the computational scheme has been discussed in detail in a theoretical paper[20] as well as in several applications[26,27] we restrict ourselves here to the minimum information required and refer to the literature for details.

We solve the problem of a deep impurity in a silicon crystal using a Green's function technique and solving a Dyson equation

$$G(\vec{r},\vec{r}',z)=G^0(\vec{r},\vec{r}',z)+\int G^0(\vec{r},\vec{r}'',z)\Delta V(\vec{r}'')G(\vec{r}'',\vec{r}',z)d^3\vec{r}'', \tag{1}$$

where $\Delta V=V-V^0$ is the difference between the one-particle potentials of the crystal containing the impurity and that of the unperturbed crystal. We have carried out a band structure calculation using the linear muffin-tin orbital method in the atomic-spheres approximation (LMTO-ASA) in order to determine the Green's function G^0 of the unperturbed crystal. Since for deep impurities the difference of the potentials $\triangle V$ has large values which, however, are restricted to a small region around the impurity we divide the crystal into a ''perturbed region'' containing the atomic spheres of the impurity atom, of a few neighboring silicon host atoms, and of space-filling interstitial spheres and into the ''unperturbed'' crystal outside this region. Our perturbed region consists of 30 atomic spheres that contain silicon atoms, of 28 empty spheres, and of the atomic sphere centered around the impurity atom. Within the perturbed region Dyson's equation is solved self-consistently, outside this region G is approximated by G^0.

From the Green's function we calculate the angular momentum and site projected density of states (DOS)

$$N_{RL,RL'}(E)=\mp\frac{1}{\pi}\lim_{\epsilon\to 0}\mathrm{Im}\mathrm{Tr}G(E\pm i\epsilon) \tag{2}$$

and the charge density of the valence electrons inside a sphere centered around the position R,

$$n_{v,R}(\vec{r}_R)=\sum_{L,L'}\int_{\infty}^{E_F}N_{RL,RL'}(E)|\varphi_{RL}(\vec{r}_R,E)|^2dE, \tag{3}$$

where the $\varphi_{RL}(\vec{r},E)$ are the solutions of the Kohn-Sham equation inside the atomic sphere around the position R. L is a shorthand notation of the angular momentum quantum numbers, lm, and $\vec{r}_R=\vec{r}-\vec{R}$.

To reduce the computational effort when solving Eq. (1) we switch to symmetry-adapted basis functions which transform according to the irreducible representations of the point group of the defect. These are constructed with a Slater projector technique[34]

$$f^{\alpha}_{\kappa\mu,\underline{Rl}}(\vec{r})=\sum_{\hat{\mathbf{R}}}\Gamma^{\alpha}_{\kappa\mu}(\hat{\mathbf{R}})^*\hat{\mathbf{R}}\phi_{RL}(\vec{r}_R)\,\theta\left(\frac{r_R}{s_R}\right). \tag{4}$$

$\Gamma^{\alpha}_{\kappa\mu}(\hat{\mathbf{R}})$ is the matrix element of the irreducible representation Γ^{α} for the point group operation $\hat{\mathbf{R}}$ of the point group of the defect. κ and μ label the rows and the columns of the matrix, respectively. R labels the different ''shells,'' i.e., the site vectors R_i that transform into each other under application of the point group operations $\hat{\mathbf{R}}$. Since the energy dependence of the $\phi_{RL}(E,\vec{r})$ is approximated by a Taylor series up to second order around some energy[35] $E_{\nu l}$, we obtain[36]

$$n^{\alpha}_{v}(\vec{r})=\sum_{\substack{R,l,l'\\ \kappa,\mu,k,j}}N^{\alpha(k)(j)}_{\underline{Rll'}}f^{\alpha,(k)}_{\kappa\kappa,\underline{Rl}}(\vec{r})f^{\alpha,(j)}_{\mu\mu,\underline{Rl'}}(\vec{r}), \tag{5}$$

where the superscripts (k) and (j) can take the values 0,1,2 and denote the function itself and its first and second derivative according to the energy, respectively. The coefficients in Eq. (5) are given by

$$N^{\alpha(k)(j)}_{\underline{Rll'}}=\frac{1}{k!\,j!}\int_{-\infty}^{E_F}N^{\alpha}_{\underline{Rll'}}(E)(E-E_{\nu,l})^k(E-E_{\nu,l'})^j dE. \tag{6}$$

The particle density given in Eq. (5) can be considered as arising from the square of some wave functions

$$|\Gamma^{\alpha},\kappa\rangle=\sum_{Rl,k}\beta^{\alpha,(k)}_{\underline{Rl}}f^{\alpha,(k)}_{\kappa\kappa,\underline{Rl}}(\vec{r}). \tag{7}$$

These wave functions can be interpreted as *defect orbitals* in the sense of covalently augmented impurity orbitals[37] since the $|\Gamma^{\alpha},\kappa\rangle$ contain both impurity and host orbitals. The coefficients β in Eq. (7) are determined by

$$\beta^{\alpha,(k)}_{\underline{Rl}}\beta^{\alpha,(j)}_{\underline{Rl'}}=N^{\alpha,(k)(j)}_{\underline{Rll'}}. \tag{8}$$

This relation turns out to be essential for the calculation of the hfi matrix elements when dealing with ground states without orbital quenching. Since we use the LSDA we have to add an additional spin index in Eqs. (2) – (7) and use spin densities instead of particle densities.

The total energy of the crystal containing the defect is calculated ignoring lattice relaxations.[20,26,27] Since the total energy is determined up to an additive constant only, we calculate the difference in energy introduced by the defect. To this we add the energy of the long-range Coulomb part of

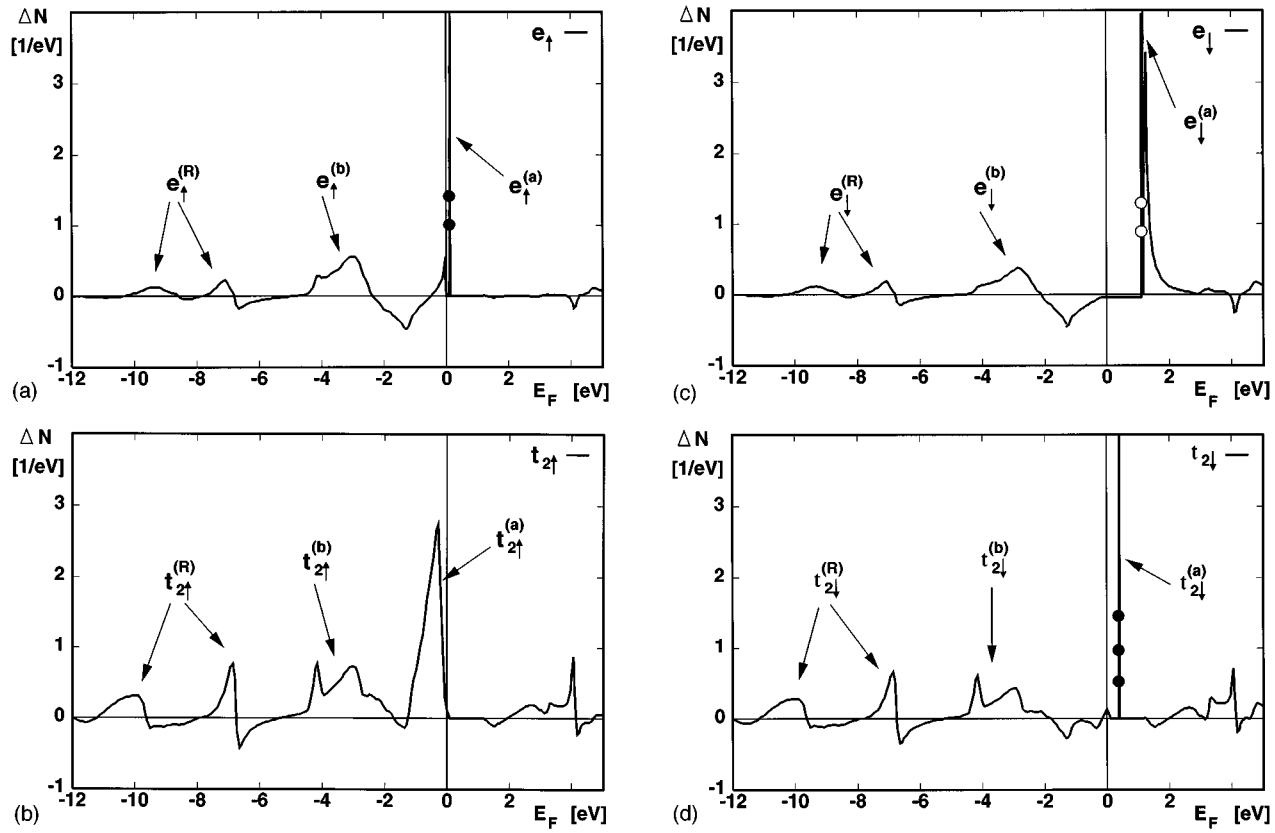

FIG. 1. Induced DOS for Si:Fe_i^0 projected onto the irreducible representations e (a),(c) and t_2 (b),(d) for both spin directions $m_s=\pm\frac{1}{2}$. We use the top of the valence band as zero for the energy and indicate occupied states in the gap by filled and unoccupied states by empty circles, respectively.

$n(0.1\ \text{eV})$ where n indicates the charge state of the impurity.[26,38] In order to compare total energies for different charge states of a defect we discuss the n-times charged defect $D^{(n)}$ plus n electrons or holes that are transferred to the Fermi level. Thus the total energy becomes a function of the Fermi level E_F,

$$E_{\text{tot}}(D^{(n)},E_F)=E^b_{\text{tot}}(D^{(n)})+nE_F, \tag{9}$$

where E^b_{tot} is the energy of the defect for a Fermi level at the valence band edge. With these total energies we calculate the electron removal energies as that position of the Fermi level for which the total energies of two charge states coincide.

B. The electronic structure of Fe_i

In agreement with several other authors we find interstitial iron in the neutral and in the positive charge states with an electron removal energy $E(+/0)=E_v+0.29$ eV. This compares reasonably well with the experimentally determined value of 0.385 eV.[4,23]

The electronic structure of TM ions in semiconductors is usually described by the model of Ludwig and Woodbury[1] (LW). Starting from the atomic configuration $[\text{Ar}]3d^n4s^m$ the $4s$ electrons are transferred to the d states, resulting in a d^{n+m} (atomic) configuration of the valence electrons for interstitial TM's. The crystal field splits the one-electron d states into e and t_2 states separated by Δ_{CF} and these in turn are further split by the exchange interaction into $e_\uparrow$ and $e_\downarrow$ states separated by $\Delta_x(e)$ and into $t_{2\uparrow}$ and $t_{2\downarrow}$ states separated by $\Delta_x(t_2)$, respectively. For interstitial TM ions in silicon the LW model predicts that the one-electron states are ordered as $\epsilon(t_{2\uparrow})<\epsilon(e_\uparrow)<\epsilon(t_{2\downarrow})<\epsilon(e_\downarrow)$. This leads to high-spin ground states, i.e., to the strong field configurations[39,40] $t_2^6e^2$ for Fe_i^0 and to $t_2^5e^2$ for Fe_i^+, respectively.

Since our symmetry-adapted one-particle orbitals (7) can be interpreted as defect orbitals in the sense of one-particle orbitals of a strong field configuration we interpret our calculated induced DOS in terms of different defect orbitals $\psi_{a_1},\psi_e,\psi_{t_2}$ with corresponding occupation numbers x,y,z of the strong field configuration $a_1^xt_2^ye^z$. Figures 1(a)–1(f) and 2(a)–2(f) show the calculated induced DOS for Si:Fe_i^0 and Si:Fe_i^+ projected onto the irreducible representations a_1,e,t_2 for both spin directions $m_s=\pm\frac{1}{2}$, respectively. We find that the peaks in the induced DOS can be divided into three groups labeled by the superscripts (a), (b), and (R). The peaks indicated by (R) form resonance structures which contain negligible charge in comparison to the structures labeled by (a) and (b).

We have analyzed the induced DOS in detail[41] with the help of projections on the impurity atomic sphere and on several atomic spheres of the neighboring ligand atoms. The analysis reveals that the peaks labeled (a) and (b) in Figs. 1 and 2 have contributions from iron d states and mainly silicon p states leading to a picture of covalent hybridized iron d states forming bonding (b) and antibonding (a) states with

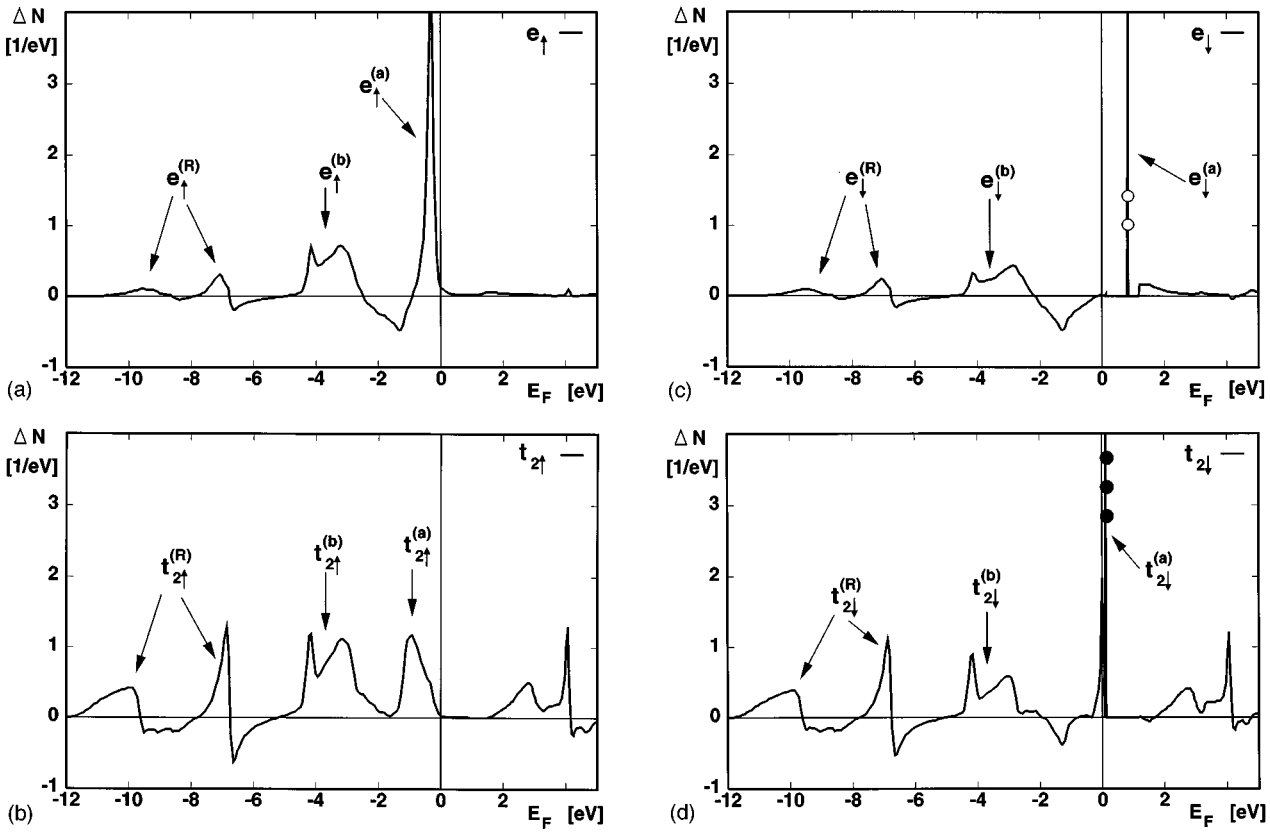

FIG. 2. Induced DOS for Si:Fe_i^+ projected onto the irreducible representations e (a),(c) and t_2 (b),(d) for both spin directions $m_s = \pm \frac{1}{2}$. We use the top of the valence band as zero for the energy and indicate occupied states in the gap by filled and unoccupied states by empty circles, respectively.

the silicon p states (see Fig. 3). In Figs. 4(a) and 4(b) we show a contour plot of the particle densities for the antibonding $t_{2\downarrow}^{(a)}$ and $e_\uparrow^{(a)}$ states of Si:Fe_i^0 in the (110) plane which demonstrate the covalent hybridization of the atomic iron d states with the ligand orbitals. For Fe_i^0 the iron d states are somewhat more localized in the antibonding orbitals with respect to the bonding states (Table I). In contrast, for Si:Fe_i^+ the d states are more localized in the bonding states (see Table I).

In order to understand the trends in the splitting and localization when going from Fe_i^0 to Fe_i^+ it is useful to reverse the order in which crystal field and exchange splitting are considered: in the following we will discuss the electronic structure starting from atomic d states that are split by the exchange interaction into $d_\uparrow$ and $d_\downarrow$ states separated by $\Delta_x(d)$. In a second step these states are further split by the crystal field with separations $\Delta_{\mathrm{CF}}^{\uparrow}$ and $\Delta_{\mathrm{CF}}^{\downarrow}$ [see Figs. 5 (a) and 5(b)]. For neutral Fe_i^0 we thus obtain $\Delta_x(d) = 0.84$ eV, $\Delta_{\mathrm{CF}}^{\uparrow} = 0.93$ eV, and $\Delta_{\mathrm{CF}}^{\downarrow} = 1.08$ eV. For iron in the positive charge state Fe_i^+ the corresponding values are $\Delta_x(d) = 1.12$ eV, $\Delta_{\mathrm{CF}}^{\uparrow} = 0.39$ eV, and $\Delta_{\mathrm{CF}}^{\downarrow} = 0.97$ eV, respectively. This order provides us with a rather simple picture of the reaction of the electronic system when we pass from Fe_i^0 to Fe_i^+. For Fe_i^0 with spin $S = 2/2$ the exchange splitting is somewhat smaller than the crystal field splittings. The states are, therefore, not spin ordered and the crystal field splitting $\Delta_{\mathrm{CF}}^{\uparrow}$ is practically equal to $\Delta_{\mathrm{CF}}^{\downarrow}$. When we go to Fe_i^+ the more attractive potential of the positive ion moves all states to lower energies. At the same time the spin is increased ($S = 1 \rightarrow S = \frac{3}{2}$) and thereby the exchange splitting is also increased. Both effects cancel in part for the $d_\downarrow$ states but cooperate to move the $d_\uparrow$ states to lower energies. Therefore

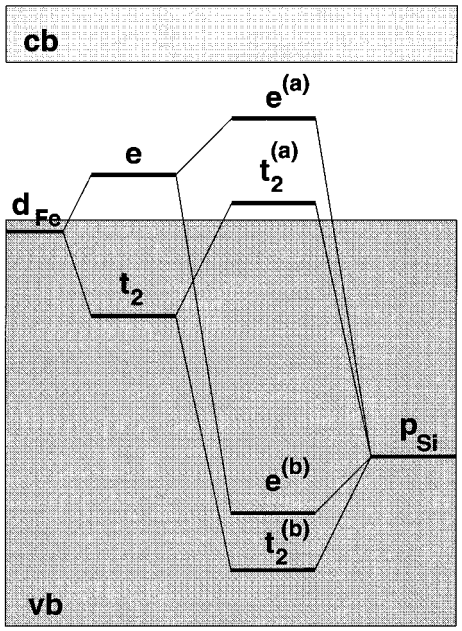

FIG. 3. Energy diagram showing the formation of bonding and antibonding states. We start with the iron d states ordered according to the LW model and neglect the exchange splitting here.

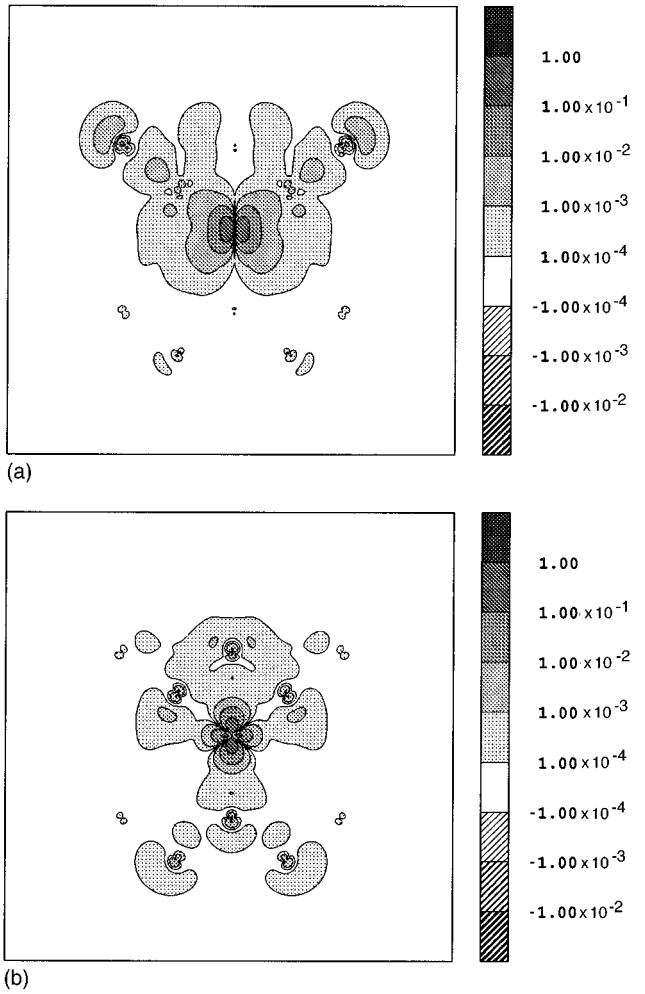

FIG. 4. Contour plot of the particle density of the antibonding $t_{2\downarrow}^{(a)}$ state (a) and of the $e_{\uparrow}^{(a)}$ state (b) in (110) for Si:Fe_i^0.

the lower-lying $d_\uparrow$ states become considerably more localized both with respect to the d states of Fe_i^0 and to the $d_\downarrow$ states of Fe_i^+. Hence the crystal field splitting $\Delta_{\mathrm{CF}}^{\uparrow}$ is drastically reduced while the crystal field splitting of the gap states $\Delta_{\mathrm{CF}}^{\downarrow}$ remains virtually unaltered, leading to the spin-ordered final states (Fig. 5).

There is a puzzling difficulty if we attempt to describe the electronic states of Fe in terms of occupation numbers: If we integrate the induced DOS projected on the irreducible representations of the point group T_d and restrict the range of integration to the ASA sphere around the interstitial iron impurity we obtain the occupation numbers

$$a_1^{0.44}t_2^{5.19}e^{2.21} \quad \text{for} \quad Fe_i^0,$$

$$a_1^{0.45}t_2^{4.95}e^{2.38} \quad \text{for} \quad Fe_i^+.$$

The same induced DOS, however, integrated with respect to all space, gives

$$a_1^{0.03}t_2^{5.75}e^{2.03} \quad \text{for Si:}Fe_i^0,$$

$$a_1^{0.09}t_2^{5.36}e^{2.19} \quad \text{for Si:}Fe_i^+.$$

Since the iron a_1 orbitals are pure s orbitals we see that the s-d transfer proposed by the LW model is nearly complete if we consider the complete defect orbitals. However, the local configurations restricted to the iron atom subspace differ significantly from the occupations of the defect orbitals: The a_1 and e orbitals are rather localized around the iron atom whereas the t_2 orbitals are more delocalized. The occupation numbers of the defect orbitals approximate the LW configurations $t_2^6e^2$ for Fe_i^0 and $t_2^5e^2$ for Fe_i^+. However, they contain small admixtures of the configurations $t_2^5e^3$ for Fe_i^0 and of $t_2^4e^3$ for Fe_i^+. Figure 6 shows a contour plot of the total induced particle density of the valence electrons for Si:Fe_i^0 in the (110) plane which indicates localization of the particle density around the iron atom with considerable redistribution of the density, which reflects considerable bonding to the surrounding ligands.

The magnetization density displayed in Fig. 7 is by far more localized than the particle density. If we introduce the local magnetic moment

$$m(X)=\int_{V(X)}[n_\uparrow(\vec{r})-n_\downarrow(\vec{r})]d^3\vec{r}, \tag{10}$$

where $n_{\uparrow,\downarrow}$ are the spin densities and $V(\mathrm{X})$ is the volume of the atomic sphere around the position X as compared to the total magnetic moment,

TABLE I. Occupation numbers of the particle densities for Si:Fe_i^0 and Si:Fe_i^+ projected onto the irreducible representations e and t_2. N_d^{Fe} is the contribution of iron d electrons and N_{tot} the total occupation number of the corresponding state.

	Fe_i^0		Fe_i^+	
State	N_d^{Fe}	N_{tot}	N_d^{Fe}	N_{tot}
$e_{\uparrow}^{(a)}$	1.16	1.70	0.81	1.27
$e_{\uparrow}^{(b)}$	0.59	0.68	0.88	0.92
$t_{2\uparrow}^{(a)}$	1.11	1.65	0.85	0.91
$t_{2\uparrow}^{(b)}$	1.08	1.13	1.48	1.68
$e_{\downarrow}^{(a)}$				
$e_{\downarrow}^{(b)}$	0.29	0.44	0.37	0.57
$t_{2\downarrow}^{(a)}$	1.33	1.99	0.85	1.25
$t_{2\downarrow}^{(b)}$	0.55	0.64	0.81	0.85

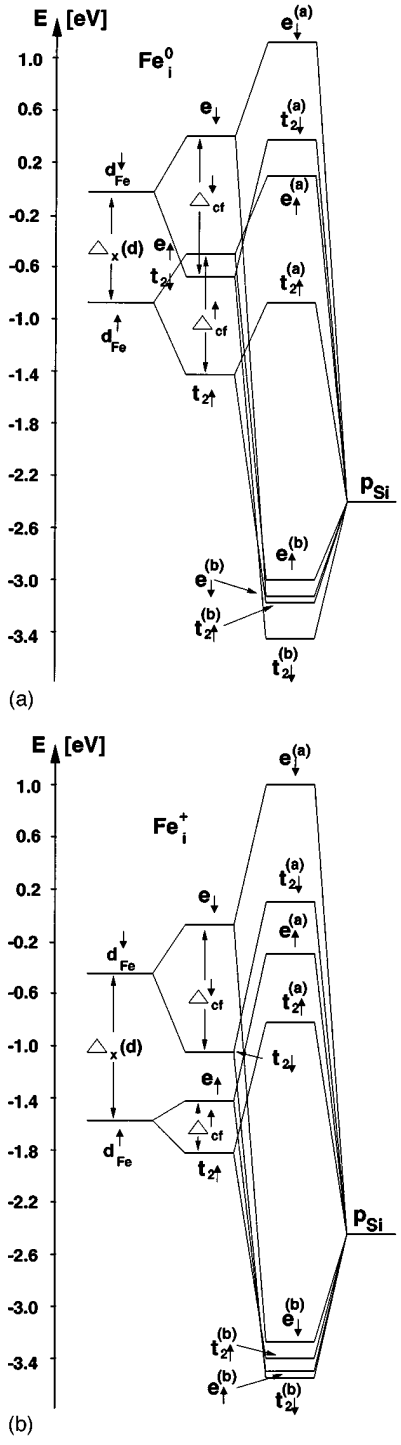

FIG. 5. Energetic positions of the one-electron states used in the covalent model for Si:Fe$_i^0$ (a) and Si:Fe$_i^+$ (b). Shown are the atomiclike iron d states that are split due to the exchange interaction and due to the crystal field (left side) which form bonding (b) and antibonding (a) defect orbital states with the silicon p states [see Eq. (7)].

$$m(\mathrm{Si}{:}X) = \int_{V_{\mathrm{pert}}} [n_{\uparrow}(\vec{r}) - n_{\downarrow}(\vec{r})]\, d^3\vec{r}, \tag{11}$$

where V_{pert} is the volume of the perturbed region, we obtain $m(\mathrm{Fe}_i^0) = 1.91\mu_B$ and $m(\mathrm{Si}{:}\mathrm{Fe}_i^0) \approx 2\mu_B$ for the neutral charge state of iron. For the positive charge state we find $m(\mathrm{Fe}_i^+) = 2.37\mu_B$ and $m(\mathrm{Si}{:}\mathrm{Fe}_i^+) = 2.76\mu_B$, respectively. Therefore for Si:Fe$_i^0$ we approximately get the total theoretical magnetic moment of $m_0(\mathrm{Fe}_i^0) = 2S = 2$ in our perturbed region (Fig. 7), and 95% of it in the iron ASA. For Si:Fe$_i^0$ we have approximately 92% of the total theoretical magnetic moment for Si:Fe$_i^+$ in the perturbed region and 80% of the total magnetic moment is found in the iron sphere. According to the total spins we can approximate the ground-state term for Si:Fe$_i^0$ as $^3A_2$ and for Si:Fe$_i^+$ as $^4T_1$, respectively.

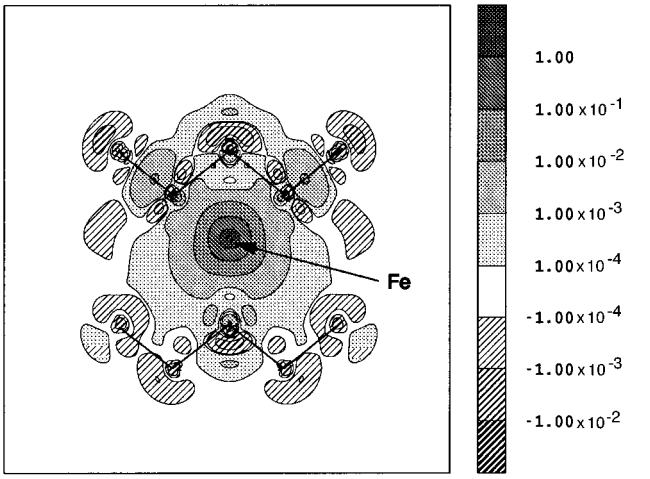

FIG. 6. Contour plot of the total induced particle density of the valence electrons for Si:Fe$_i^0$ in (110).

III. CALCULATION OF THE HYPERFINE INTERACTIONS

A. Theory

The Hamiltonian representing the hfi of N valence electrons of the defect with M nuclei (impurity and host nuclei) reads

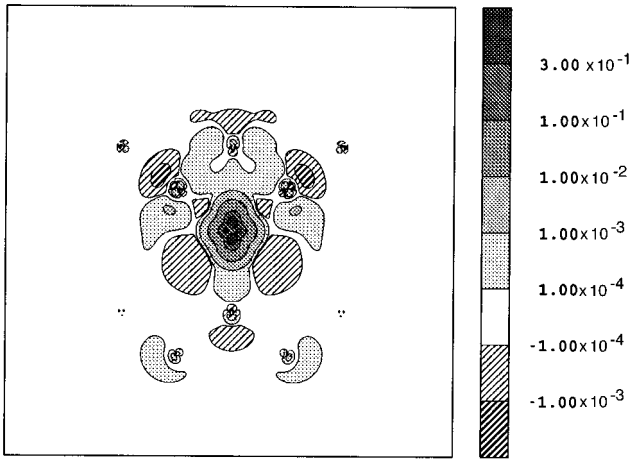

FIG. 7. Contour plot of the magnetization density of the valence electrons for Si:Fe$_i^0$ in (110).

TABLE II. Comparison of calculated and measured hfi data (in MHz) for Si:Fe_i^0. The hfi data for the Si ligands are taken from ENDOR measurements (Refs. 7 and 8) and the hfi constant for Fe is determined by EPR measurements (Ref. 1). In the last column we show the calculated contact data from Katayama-Yoshida and Hamada (Ref. 28), who carried out a supercell calculation. In order to overcome the ambiguity of the results for ligands of supercell calculations these data have been scaled with the experimental values.

	Refs. 7 and 8		This work		Ref. 28
Position	a_{expt}	$b_{\text{expt}}/b'_{\text{expt}}$	a	b/b'	a_{calc}
$Fe^0(0,0,0)$	± 20.94		-15.2		
Si(1,1,1)	0.157	1.402	3.032	1.504	-0.15
Si(1,1,$\overline{3}$)	-3.870	$-0.434/0.068$	-3.887	$-0.448/0.035$	-3.60
Si(2,0,0)	-4.641	$-0.799/-0.514$	-12.981	$-0.679/0.040$	-16.66
Si(2,2,2)	3.244	-0.156	3.945	-0.242	$+2.79$
Si(2,2,$\overline{2}$)	0.776	-0.196	1.074	-0.143	$+0.67$

$$H_{\text{hfi}}=\sum_{j=1}^{M}\gamma_j\sum_{i=1}^{N}\left(\frac{8\pi}{3}\delta(\vec{r}_{ij})\vec{s}_i+\frac{\vec{l}_i}{r_{ij}^3}+\frac{3(\vec{r}_{ij}\cdot\vec{s}_i)\vec{r}_{ij}-r_{ij}^2\vec{s}_i}{r_{ij}^5}\right)\vec{I}_j H_{\text{CP}}, \tag{12a}$$

$$\gamma_j=\frac{\mu_0}{4\pi}2g_N^j\mu_N\mu_B, \quad \vec{r}_{ij}=\vec{r}_i-\vec{R}_j,$$

where the nuclei with nuclear spin $\vec{I}_j$ and with the g factor g_N^j are at the positions $\vec{R}_j$. H_{CP} takes into account the core polarization[42,43]

$$H_{\text{CP}}=\sum_j A_{\text{CP}}^j\vec{I}_j\cdot\vec{S}, \tag{12b}$$

$$A_{\text{CP}}^j=\frac{8\pi}{3}\gamma_j\frac{1}{2S}\sum_i\{|\varphi_{i\uparrow}(\vec{R}_j)|^2-|\varphi_{i\downarrow}(\vec{R}_j)|^2\}.$$

Since our one-particle Kohn-Sham equation is based on a Dirac equation neglecting spin-orbit interaction we calculate the Fermi contact contributions arising from (12) as the average of the squared one-particle functions over a region near the nucleus whose diameter is the Thomson radius $r_T=Ze^2/mc^2$ (Ref. 44). To determine the hfi of the defect electrons with the magnetic nuclei we calculate the matrix elements of (12) in first order perturbation theory.

B. Results

1. Si:Fe_i^0

The total energy calculations have shown that the ground state of Si:Fe_i^0 is well approximated by $^3A_2$. Therefore we have orbital quenching and calculate the hfi matix elements directly with the help of the magnetization density[45]

$$m(\vec{r})=n_\uparrow(\vec{r})-n_\downarrow(\vec{r})$$

to

$$\mathbf{H}=\sum_j a_j\{\vec{S}\cdot\vec{I}_j+\vec{S}\cdot\mathbf{B}\cdot\vec{I}_j\}, \tag{13a}$$

$$a_j=\frac{1}{2S}\frac{8\pi}{3}\gamma_j\int m(\vec{r}+\vec{R}_j)\delta(\vec{r})d^3\vec{r}, \tag{13b}$$

$$(B_j)_{kl}=\frac{1}{2S}\gamma_j\int m(\vec{r}+\vec{R}_j)\frac{3x_kx_l-r^2\delta_{kl}}{r^5}d^3\vec{r}. \tag{13c}$$

Here $n_\uparrow(\vec{r})$ and $n_\downarrow(\vec{r})$ are the spin densities calculated in the DFT-LSDA (including the core polarizations). The isotropic constants a_j are directly related to the Fermi contact interaction, the matrices $\mathbf{B}_j$ characterize the angular dependent parts of the spin Hamiltonian (13a). To evaluate the integral (13c) which extends over all space we make use of the LMTO-ASA concept and approximate[46]

$$\mathbf{B}_j=\frac{1}{2S}\gamma_j\int_{V_s(\vec{R}_j)}m(\vec{r}+\vec{R}_j)\frac{3\vec{r}\otimes\vec{r}-r^2\mathbf{1}}{r^5}d^3\vec{r} \tag{14a}$$

$$+\frac{1}{2S}\gamma_j\sum_i m(\vec{R}_i)\frac{3\vec{R}_{ij}\otimes\vec{R}_{ij}-R_{ij}^2\mathbf{1}}{R_{ij}^5}, \tag{14b}$$

where $\vec{R}_{ij}=\vec{R}_i-\vec{R}_j$,

$$m(\vec{R}_i)=\int_{V_s(\vec{R}_i)}m(\vec{r})d^3\vec{r},$$

and $V_s(\vec{R}_i)$ is the volume of the atomic sphere of radius s around the lattice point $\vec{R}_i$. Since the matrices $\mathbf{B}_j$ are traceless they are transformed into their eigensystem and the eigenvalues are parametrized as $2b$, $-b+b'$, $-b-b'$, such that $2b$ is the largest eigenvalue.

In Table II we compare our total calculated hfi data summarized by a, b, and b' with experimental hfi data which have been measured in ENDOR (Refs. 7 and 8) (for the Si ligands) and in EPR (Ref. 1) (for Fe) experiments. For the ENDOR data relative signs between a, b, and b' are known, for the EPR data only absolute values can be given.

Our calculated ligand hfi data show excellent agreement with the measured data for the anisotropic constants b and fair agreement for the isotropic constants a. We get large deviations between calculated and measured data for the contact data of the first two inner shell positions Si(1,1,1) and Si(2,0,0). The major part of the magnetization density, however, is related to the constants b. Therefore our calculated

TABLE III. Decomposition of the calculated hfi contact data (in MHz) for Si:Fe_i^0 into contributions from various one-particle states and from the core polarization.

Position	a_e	a_{t_2}	a_{gap}	a_{VB}	a_{CP}	a_{tot}
Fe^0(0,0,0)	0	0	0	12.49	−27.66	−15.17
Si(1,1,1)	0	−0.2947	−0.2947	2.563	0.763	3.032
Si(1,1,$\overline{3}$)	−5.666	−1.676	−7.342	3.4279	0.0274	−3.887
Si(2,0,0)	−10.995	−0.023	−11.018	−2.002	0.0396	−12.981
Si(2,2,2)	0	−18.824	−18.824	22.753	0.0158	3.945
Si(2,2,$\overline{2}$)	0	−0.474	−0.474	1.556	−0.008	1.074

magnetization density shown in Fig. 7 is essentially correct even if there are some serious discrepancies with respect to the ligand contact hfi. The calculated total hfi data arise from contributions of the gap states, from the states in the valence bands, and from the contact terms of the core states (core polarization). These decompositions are shown in Table III for the Fermi contact constants a and in Table IV for the matrices **B**. In the last column of Table IV we show the eigendirections of the largest eigenvalue $2b$ of **B**. The first two columns give the local contributions of the magnetization density according to (14a), in the last column we also include the point-dipole part of (14b). Obviously the good agreement between calculated and measured data is only obtained if both parts—local and point-dipole parts—are taken into account.

The contact hfi data for the interaction with the central Fe nucleus (Table III) have two major contributions from the valence band polarization and from the core polarization.[11] Both have opposite signs and in the self-consistent cycle influence each other, thus strongly impeding the convergence. The data of Table III show that the core polarizations caused by the defect electrons are large for the iron and for the first silicon neighbor shell only. The contact densities correspond to very small fractions of s densities of the magnetization density and should be rather sensitive to lattice relaxations. Such relaxations are predicted to occur as a symmetric *breathing mode relaxation* with large relaxations for the first two shells of silicon atoms for interstitial TM ions in silicon.[21,25,47] This may be the reason for the fact that the deviations of the calculated contact hfi data for the close Si (1,1,1) and Si(2,0,0) ligands as compared to the experimental data are quite large while theoretical and experimental contact hfi data agree quite nicely for the more distant ligand shells.

2. Si:Fe_i^+

Based on our total energy calculations we approximate the electronic ground-state term for Si:Fe_i^+ by $^4T_1(t_2^5e^2)$. The spin-orbit interaction splits this term into the sublevels $\Gamma_6(j=\frac{1}{2})$, $\Gamma_8(j=\frac{3}{2})$, $\Gamma_7(j=\frac{5}{2})$, and $\Gamma_8(j=\frac{5}{2})$. The sublevels $\Gamma_7(\frac{5}{2})$, $\Gamma_8(\frac{5}{2})$ are degenerate in first order perturbation theory and the $\Gamma_6(\frac{1}{2})$ sublevel is the ground state.[10,31–33,39,40,48] The Γ_i denote the irreducible representations of the cubic double group T_d^D and j indicates the total angular momentum resulting from the coupling of the total spin $S=\frac{3}{2}$ with the fictitious orbital angular momentum $\tilde{l}=1$ attributed to the orbital triplet T_1 due to the Wigner-Eckart theorem.[39,40] Since the ground-state functions

$$|\Gamma_{6\pm\frac{1}{2}}\rangle = \sqrt{6}\,|^4T_1(\pm\overline{1})(\mp\tfrac{1}{2})\rangle - \frac{1}{\sqrt{3}}|^4T_1(\overline{0})(\pm\tfrac{1}{2})\rangle + \frac{1}{\sqrt{2}}|^4T_1(\mp\overline{1})(\pm\tfrac{3}{2})\rangle \tag{15}$$

are eigenfunctions of the spin-orbit interaction which is not taken into account in our total energy calculations we approximate the many-particle functions[49] $|^4T_1(\overline{m_{\tilde{l}}})(M_S)\rangle$ as Slater determinants of the hole configuration t_2e^2,

$$|^4T_1(\overline{m_{\tilde{l}}})(M_S)\rangle = |m_{\tilde{l}}\theta\epsilon||M_S\rangle. \tag{16}$$

TABLE IV. Decomposition of our calculated anisotropic hfi constants b and b' for Si:Fe_i^0 (in MHz). The vector $\vec{\nu}$ indicates the eigendirection of $2b$. The indices g and VB indicate the inclusion of the gap states (g) and of the states that occur in the valence bands (VB) to the magnetization density. The index tot indicates the inclusion of the contribution from (14b).

Position	$b_g/\lvert b'_g\rvert$	$b_{g+\text{vb}}/\lvert b'_{g+\text{VB}}\rvert$	$b_{\text{tot}}/\lvert b'_{\text{tot}}\rvert$	$\vec{\nu}$
Fe^0(0,0,0)	0.0	0.0	0.0	
Si(1,1,1)	1.538	2.659	1.504	[111]
Si(1,1,$\overline{3}$)	−0.844/0.175	−0.306/0.009	−0.449/0.035	$\angle[111]=-83.3°$
Si(2,0,0)	−1.630/0.068	0.074/0.010	−0.679/0.040	[100]
Si(2,2,2)	2.754	−0.0826	−0.2423	[111]
Si(2,2,$\overline{2}$)	$\approx$ 0.0	−0.003	−0.144	[111]

TABLE V. Decomposition of all calculated hfi matrix elements (for Si:Fe_i^+) into contributions from the core polarization (CP), from the Fermi contact interaction (c), from the orbital angular momentum (l), from the local parts of the dipole-dipole interaction (d), and from the dipole-dipole interaction with the magnetization density localized around the iron atom (dd).

Site	Tensor element	α					
		CP	c	l	d	dd	tot
Fe(0,0,0)	a_{xx}^{α}	−20.73		48.04	−2.29		25.06
Si(1,1,1)	a_{xx}^{α}	−0.695	−1.876	2.506	−0.063		−0.128
	a_{xy}^{α}		0.376	1.345	2.829	−1.517	3.033
Si(2,2,2)	a_{xx}^{α}	−2.766	2.000	1.197	0.770		1.201
	a_{xy}^{α}		−0.400	−0.794	−0.847	−0.190	−2.231
Si(2,2,$\overline{2}$)	a_{xx}^{α}	−0.011	0.175	−0.073	−0.036		0.055
	a_{xy}^{α}		−0.035	−0.043	0.016	−0.189	−0.251
Si(2,0,0)	a_{xx}^{α}	7.389	−11.82		−0.891	−1.969	−7.291
	a_{yy}^{α}	7.389	−11.26		0.474	−0.984	−4.281
Si(1,1,$\overline{3}$)	a_{xx}^{α}	−3.187	−1.738	−0.247	−0.002	0.157	−5.008
	a_{xy}^{α}		0.123	−0.020	−0.388	−0.059	−0.344
	a_{xz}^{α}		0.123	0.050	0.226	0.177	0.576
	a_{yx}^{α}		0.123	−0.241	−0.366	−0.059	−0.543
	a_{yy}^{α}	−3.187	−1.738	−0.036	0.088	0.157	−4.706
	a_{yz}^{α}		0.123	0.050	0.240	0.177	0.590
	a_{zx}^{α}		0.123	−0.340	0.258	0.177	0.218
	a_{zy}^{α}		0.123	−0.020	0.205	0.177	0.485
	a_{zz}^{α}	−3.187	−1.738	−0.143	−0.163	0.069	−4.906

Here the $m_{\tilde{l}}$ are the one-particle eigenfunctions[50] of the fictitious orbital angular momentum $\tilde{l}=1$: $|\pm\tilde{1}\rangle = \mp 1/\sqrt{2}(t_{2x}\pm it_{2y}), |\tilde{0}\rangle = t_{2z}$ with t_{2x}, t_{2y}, t_{2z}, and θ, ϵ transforming according to the first and second (and third) column of the irreducible representations t_2 and e of the point group T_d, respectively. The notation $|abc|$ indicates a Slater determinant of the three orbitals a, b, and c and $|M_S\rangle$ is a symmetric three-particle spin function.[10]

We have approximated the t_2 and e one-particle functions by the defect orbitals (7) [restricted to the $k=0$ contribution of Eq. (7) only]. Since we deal with a t_2e^2 hole configuration we approximate the coefficients $\beta_{Rl}^{\alpha,(0)}$ with the help of the magnetization density calculated in the LSDA-DFT (Ref. 51) and take

$$\beta_{Rl}^{\alpha,(0)}\beta_{Rl'}^{\alpha,(0)} = N_{Rll'\uparrow}^{\alpha,(0),(0)} - N_{Rll'\downarrow}^{\alpha,(0),(0)}. \tag{17}$$

We therefore take the localization of a t_2 and an e hole around a lattice site R as coefficient $\beta_{Rl}^{\alpha,(0)}$ in our t_2 and e defect orbitals (7), respectively. With the assignment (17) we take into account covalent effects as well as the spin-polarization effects of our LSDA-DFT magnetization density.[52]

For the Γ_6 ground state we have calculated the hfi matrix elements of (12) with the iron nucleus and with five silicon nuclei centered at Si(1,1,1), Si(2,2,2), Si(2,2,$\overline{2}$) (which represent shells of four equivalent ligands with trigonal symmetry), at Si(2,0,0) (which represents a shell of six equivalent ligands with rhombic symmetry), and at Si(1,1,$\overline{3}$) (which represents a shell of 12 equivalent ligands with monoclinic symmetry). In order to compare our results with experimental data from EPR (Ref. 1) and ENDOR (Ref. 10) measurements we have to transform our matrix elements into those of a spin Hamiltonian for an effective spin $S'=\frac{1}{2}$,

$$\mathbf{H} = \vec{S}'\cdot\mathbf{A}^{\mathrm{Fe}}\cdot\vec{I}_{\mathrm{Fe}} + \sum_{j}^{\mathrm{Si}} \vec{S}'\cdot\mathbf{A}^{j}\cdot\vec{I}_{j}. \tag{18}$$

According to first order perturbation theory the effective spin $S'=\frac{1}{2}$ is identical to the total angular momentum of the ground state $j=\frac{1}{2}$. If we abbreviate $|\Gamma_6\pm\frac{1}{2}\rangle = |\pm\rangle$ and

$$\vec{N}^{j} = \gamma_j \sum_{i=1}^{3} \left(\frac{8\pi}{3}\delta(\vec{r}_{ij})\vec{s}_i + \frac{\vec{l}_i}{r_{ij}^3} + \frac{3(\vec{r}_{ij}\cdot\vec{s}_i)\vec{r}_{ij} - r_{ij}^2\vec{s}_i}{r_{ij}^5} \right) + A_{\mathrm{CP}}^{j}\vec{S} \tag{19}$$

[where the notations are taken from Eq. (12)] the matrix elements A_{kl}^{j} of (18) are related to those of (12) by $A_{kx}^{j} + iA_{ky}^{j} = 2\langle -|N_k^j|+\rangle$ and $A_{kz}^{j} = 2\langle +|N_k^j|+\rangle$. Details of the calculation can be found in the Appendix.

As was pointed out by van Kooten, Sieverts, and Ammerlaan,[10] there is no longer a one-to-one correspondence between the contact term contributions and the isotropic hfi constants [and likewise between the dipole-dipole interaction and the angular dependent parts of (18),

TABLE VI. Comparison of measured (Ref. 10) and calculated hfi data (in MHz) for Si:Fe_i^+.

	a_{expt}	b_{expt}	b'_{expt}	a	b	b'
$Fe^+(0,0,0)$	± 8.97			25.06 [a]		
				-6.49 [b]		
Si(1,1,1)	0.087	1.231		-0.128	3.033	
Si(2,2,2)	0.764	-0.226		1.201	-2.231	
Si(2,2,$\bar{2}$)	?	?	?	0.055	-0.251	
Si(2,0,$\bar{0}$)	-7.529	-0.738	0.460	-5.351	-0.970	
Si(1,1,$\bar{3}$)	-3.927	-0.518	0.159	-4.873	-0.462	0.170

[a]Calculated with an orbital reduction factor which is only due to covalent effects.
[b]Here we use $g_{\tilde{l}}^{EPR}$.

respectively] if we switch from a description with the ''true'' spin $S=\frac{3}{2}$ to a description with an effective spin $S'=\frac{1}{2}$. Table V shows a decomposition of our results for all calculated (independent) hfi matrix elements. For the hfi with the iron nucleus we get an isotropic hfi matrix with a total value of 25.06 MHz which deviates significantly from the measured EPR data[1] of ± 8.87 MHz. This discrepancy can be understood if we go one step back and calculate the g value measured in EPR. For the ground state we obtain

$$g(\Gamma_6)=\tfrac{5}{3}g_s-\tfrac{2}{3}g_{\tilde{l}}, \tag{20}$$

where $g_s\approx 2$ and $g_{\tilde{l}}$ are the g factors of the electron spin and of the orbital angular momentum, respectively. If the ground-state term for Fe_i^+ is approximated by $^4T_1(^4F)$ (arising from the weak field coupling term ^4F) $g_{\tilde{l}}$ has the value $g_{\tilde{l}}^{WF}=-\frac{3}{2}$. For the strong field coupling limit (without covalent effects) as $^4T_1(t_2^5e^2)$ we have $g_{\tilde{l}}^{SF}=-1$. This leads to $g^{WF}(\Gamma_6)=\frac{13}{3}$ and $g^{SF}(\Gamma_6)=\frac{12}{3}=4$. However, the value determined by EPR is $g^{EPR}=3.524$, which corresponds to $g_{\tilde{l}}=-0.286$. This large deviation between calculated and measured g factors has been attributed to two effects in the literature: to covalent hybridization of the iron d states with silicon ligand orbitals[23] and with iron p states or alternatively to a dynamical Jahn-Teller effect as a Ham effect.[30]

Covalent hybridization is taken into account by our defect orbitals. For the strong field term $^4T_1(t_2^5e^2)$ we calculate $g_{\tilde{l}}=-\beta_0^2$ using the same approximations as for the hfi matrix elements. According to our calculations p-d mixing of iron states is negligible. If we compare our value of $g_{\tilde{l}}\approx -0.83$ with the value inferred from the EPR data $g_{\tilde{l}}^{EPR}=-0.286$ we see that our localization of the t_2 magnetization density would be about a factor 3 too large to account for the reduction. Since we have learned from the calculated hfi data for $Si:Fe_i^0$ that our self-consistent magnetization densities are in excellent agreement with the ones ''seen'' in EPR we expect the same for $Si:Fe_i^+$. We additionally will show in a forthcoming paper on iron-acceptor pair defects in silicon that it is possible to calculate localization factors from the magnetization density which are in good agreement with the measured data.[53] Therefore we conclude that the rather small orbital g value $g_{\tilde{l}}$ measured in EPR is subject to covalent hybridization *and* to a Ham effect which introduces an additional reduction factor for the matrix elements of the orbital angular momentum of the iron atom. If we apply this reduction factor to our hfi matrix elements, the orbital contribution reduces by about a factor 3, leading to a total hfi value $a_{Fe}=-6.49$ MHz (as indicated in Table V) in fair agreement with the EPR data.

The comparison of our calculated hfi data for the silicon ligands with ENDOR data[10] (see Table VI) shows that except for the isotropic constant for Si(1,1,1) all calculated data have the same sign and are of the same order of magnitude as the measured data. The discrepancy for $a_{Si(1,1,1)}$ may be due to the rather small total value which arises from the combination of large single contributions (see Table V). As was the case for $Si:Fe_i^0$, our calculated hfi data for $Si:Fe_i^+$ agree much better with experimental data for the more distant ligands, which again might indicate the influence of lattice relaxations for the inner ligand shells. We note that our calculated hfi matrix for Si(1,1,$\bar{3}$) is *not* symmetric as there is no symmetry constraint for this ligand which would forbid such asymmetry. This is another example of asymmetric hfi matrices for defects in silicon which shows that asymmetric hfi matrices are not only found for defects with a lower symmetry[54,55] but do occur for highly symmetric defects as well.[56] We note that the evaluation of the ENDOR experiments[10] was based on the invalid assumption that the hfi matrix is symmetrical for the ligand Si(1,1,$\bar{3}$) so that it might be difficult to compare measured and calculated data.

IV. CONCLUSIONS

We have shown that the trends of the exchange and crystal field splittings of $Si:Fe_i^0$ and $Si:Fe_i^+$ can be understood if one considers the exchange splitting first. We have also shown that for the case of $Si:Fe_i^0$ one can obtain spin densities from *ab initio* LSDA-DFT calculations that result in hf interactions with the Fe nucleus and also with several Si ligand nuclei in close agreement with experimental hfi data. For the contact interaction with the Si(1,1,1) and Si(2,0,0) shells we find a significant discrepancy between our calculated results and the experimental data. As this discrepancy corresponds to a slight error in the s-like spin admixture at these ligands only, we conclude that our spin densities are essentially correct. However, the calculated isotropic hfi with the more distant Si ligands agrees very closely with the experimental data. We therefore argue that the experimental results could be influenced by a breathinglike lattice distortion which is not included in our calculation. The agreement

TABLE VII. Iron d functions transforming according to the irreducible representations t_2 and e of the point group T_d.

j	$\lvert t_{2j}\rangle_{\mathrm{Fe}}$	j	$\lvert e_j\rangle_{\mathrm{Fe}}$
x	$\lvert yz\rangle$	θ	$\lvert 3z^2-r^2\rangle$
y	$\lvert xz\rangle$	ϵ	$\lvert x^2-y^2\rangle$
z	$\lvert xy\rangle$		

between experimental and calculated data for the anisotropic hfi (and also for the isotropic part of the hfi with the more distant ligand shells) allows one to assign ligand shells to ENDOR results in a unique way.

The hfi data for the Si:Fe_i^+ deep defect cannot be obtained in the same way from the spin densities because of incomplete quenching of the orbital momentum in this case. We have, therefore, constructed many-particle wave functions which reflect the localization properties of the magnetization densities obtained from the LSDA-DFT calculations. We show that with these functions we still do not obtain the hfi with the central Fe nucleus in any reasonable agreement with the experimental data. We must infer in addition a dynamical Jahn-Teller effect as a Ham effect in order to obtain consistent hfi data in agreement with experimental data. A very strong argument for the presence of this effect comes from the gyromagnetic ratio as measured experimentally by EPR: the observed value of $g_l^{\sim} = -0.286$ is in no way compatible with the p-d mixing ratio for iron as observed in our calculations for which we would obtain $g_l^{\sim} = -0.83$. From the close agreement of our hfi results with experimental data in the case of Si:Fe_i^0 we conclude that the spin-density distribution obtained by the LSDA-ASA calculation is essentially correct. We have found no reason to assume that the same agreement should be absent in the case of Si:Fe_i^+. If we therefore conclude that the p-d mixing ratio for Si:Fe_i^+ cannot be discounted as unrealistic there is little alternative but a Ham effect to explain the value of $g_l^{\sim}$ observed experimentally. The comparison of the hfi data calculated including the reduction factor of the Ham effect (Table VI) with the experimental data shows that a consistent set of data is obtained.

ACKNOWLEDGEMENT

Financial support from the Deutsche Forschungsgemeinschaft is gratefully acknowledged.

APPENDIX: HYPERFINE MATRIX ELEMENTS FOR Si:Fe_i^+

We use the following linear combinations of one-particle orbitals as defect orbitals (7):

$$\lvert t_{2\alpha}\rangle = \beta_0 \lvert t_{2\alpha}\rangle_{\mathrm{Fe}} + \sum_{k=1}^{3} \beta_k \lvert f_k^{\alpha}\rangle + \sum_{m=1}^{2} \gamma_m \lvert g_m^{\alpha}\rangle + \sum_{r=1}^{4} \delta_r \lvert h_r^{\alpha}\rangle + \text{empty spheres}, \quad \alpha = x,y,z, \tag{A1a}$$

$$\lvert e_{\alpha}\rangle = \beta_{00} \lvert e_{\alpha}\rangle_{\mathrm{Fe}} + \beta_4 \lvert f_4^{\alpha}\rangle + \sum_{m=3}^{4} \gamma_m \lvert g_m^{\alpha}\rangle + \sum_{r=5}^{7} \delta_r \lvert h_r^{\alpha}\rangle + \text{empty spheres}, \quad \alpha = \theta, \epsilon. \tag{A1b}$$

For convenience we introduce the new abbreviations β_k, γ_m, δ_r for the coefficients β_{Rl}^{α}. The functions $\lvert t_{2\alpha}\rangle_{\mathrm{Fe}}$, $\lvert e_{\alpha}\rangle_{\mathrm{Fe}}$, $\lvert f_k^{\alpha}\rangle$, $\lvert g_m^{\alpha}\rangle$, and $\lvert h_r^{\alpha}\rangle$, which are linear combinations of site-centered one-particle orbitals $\lvert L\rangle_R = \varphi_{RL}(\vec{r}_R)\Theta(r_R/s_R)$, are given in Tables VII–X,[57] the sites around which the atomic spheres are centered are given in Table XI.

Using Eqs. (15) and (16) we calculate the hfi matrix elements $\langle -\lvert N_k^j\rvert + \rangle$, $\langle +\lvert N_k^j\rvert + \rangle$ of Eq. (19). Since the operator N_k^j is a sum of one-particle operators,

$$N_k^j = \sum_{i=1}^{3} n_k^j(i), \tag{A2}$$

TABLE VIII. Unnormalized, symmetry-adapted linear combinations of ligand functions [f_k^{α}, see Eq. (A1)] for trigonal shells of four silicon atoms. We use the notation $\lvert L\rangle_R$, where L denotes a cubic harmonic and R numbers the four site positions building up the shell (see Table XI). Where two signs $\pm$ and $\mp$ are given the first one applies for Si(1,1,1) and Si(2,2,2), the second one applies for Si(2,2,2).

α	k	$\lvert f_k^{\alpha}\rangle$
x	1	$\lvert s\rangle_1 - \lvert s\rangle_2 + \lvert s\rangle_3 - \lvert s\rangle_4$
	2	$\lvert x\rangle_1 + \lvert x\rangle_2 + \lvert x\rangle_3 + \lvert x\rangle_4$
	3	$\lvert y\pm z\rangle_1 + \lvert -y\pm z\rangle_2 - \lvert y\pm z\rangle_3 + \lvert y\mp z\rangle_4$
y	1	$\lvert s\rangle_1 + \lvert s\rangle_2 - \lvert s\rangle_3 - \lvert s\rangle_4$
	2	$\lvert y\rangle_1 + \lvert y\rangle_2 + \lvert y\rangle_3 + \lvert y\rangle_4$
	3	$\lvert x\pm z\rangle_1 - \lvert x\pm z\rangle_2 + \lvert -x\pm z\rangle_3 + \lvert x\mp z\rangle_4$
z	1	$\pm\lvert s\rangle_1 \mp \lvert s\rangle_2 \mp \lvert s\rangle_3 \pm \lvert s\rangle_4$
	2	$\lvert z\rangle_1 + \lvert z\rangle_2 + \lvert z\rangle_3 + \lvert z\rangle_4$
	3	$\pm\lvert x+y\rangle_1 \pm \lvert x-y\rangle_2 \pm \lvert -x+y\rangle_3 \mp \lvert x+y\rangle_4$
θ	4	$\lvert x+y\mp 2z\rangle_1 + \lvert -x+y\pm 2z\rangle_2 + \lvert x-y\pm 2z\rangle_3 - \lvert x+y\pm 2z\rangle_4$
ϵ	4	$\lvert -x+y\rangle_1 + \lvert x+y\rangle_2 - \lvert x+y\rangle_3 + \lvert x-y\rangle_4$

TABLE IX. Unnormalized, symmetry-adapted linear combinations of ligand functions [g_k^α, see Eq. (A1)] for a rhombic shell of silicon atoms. We use the notation $|L\rangle_R$, where L denotes a cubic harmonic and R labels the six site positions building up the shell. (See Table XI.)

α	m	$\lvert g_m^\alpha\rangle$
x	1	$\lvert s\rangle_{17}-\lvert s\rangle_{22}$
	2	$\lvert x\rangle_{17}+\lvert x\rangle_{22}$
y	1	$\lvert s\rangle_{18}-\lvert s\rangle_{21}$
	2	$\lvert y\rangle_{18}+\lvert y\rangle_{21}$
z	1	$\lvert s\rangle_{19}-\lvert s\rangle_{20}$
	2	$\lvert z\rangle_{19}+\lvert z\rangle_{20}$
θ	3	$\lvert s\rangle_{17}+\lvert s\rangle_{18}-2\lvert s\rangle_{19}-2\lvert s\rangle_{20}+\lvert s\rangle_{21}+\lvert s\rangle_{22}$
	4	$\lvert x\rangle_{17}+\lvert y\rangle_{18}-2\lvert z\rangle_{19}+2\lvert z\rangle_{20}-\lvert y\rangle_{21}-\lvert x\rangle_{22}$
ϵ	3	$-\lvert s\rangle_{17}+\lvert s\rangle_{18}+\lvert s\rangle_{21}-\lvert s\rangle_{22}$
	4	$-\lvert x\rangle_{17}+\lvert y\rangle_{18}-\lvert y\rangle_{21}+\lvert x\rangle_{22}$

the three-particle matrix elements reduce to sums of one-particle matrix elements. Carrying out the spin integrations we are left with spatial integrals of the form

$$ {}_R\langle L|n_k^j|L'\rangle_{R'}. \tag{A3}$$

Since the orbitals $|L\rangle_R$ are restricted to the atomic sphere around the site R, we have one-, two-, and three-center integrals. The one-center integrals ($R=R_j=R'$) are calculated exactly. The only two-center integrals ($R=R'\neq R_j$, $R=R_j\neq R'$, $R'=R_j\neq R$) that are taken into account are the integrals of the dipole-dipole interaction with $R=R'=0$.[58] These are approximated by

$$\langle L|a_{lk}^j|L'\rangle \approx \gamma_j \frac{3(-R_j)_l(-R_j)_k - R_j^2\delta_{lk}}{R_j^5}\beta_{\mathrm{Fe}}^2\delta_{LL'}, \tag{A4}$$

where β_{Fe} is β_0 or β_{00} and

$$a_{lk}^j=\gamma_j\frac{3X_lX_k-R^2\delta_{lk}}{R^5},\quad X_l=(\vec{r}-\vec{R}_j)\cdot\vec{e}_l, R=|\vec{r}_{R_j}|.$$

All three-center integrals ($R\neq R_j\neq R'$) vanish.

For convenience we introduce the following parameters:

TABLE X. Unnormalized, symmetry-adapted linear combinations of ligand functions [h_k^α, see Eq. (A1)] for a monoclinic shell of silicon atoms. We use the notation $|L\rangle_R$, where L denotes a cubic harmonic and R labels the 12 site positions building up the shell. (See Table XI.)

α	r	$\lvert h_r^\alpha\rangle$
x	1	$\lvert s\rangle_5+\lvert s\rangle_7+\lvert s\rangle_9-\lvert s\rangle_{11}-\lvert s\rangle_{13}+\lvert s\rangle_{14}-\lvert s\rangle_{15}-\lvert s\rangle_{16}$
	2	$\lvert x\rangle_5+\lvert x\rangle_7+\lvert x\rangle_9+\lvert x\rangle_{11}+\lvert x\rangle_{13}+\lvert x\rangle_{14}+\lvert x\rangle_{15}+\lvert x\rangle_{16}$
	3	$\lvert y\rangle_5+\lvert z\rangle_7-\lvert z\rangle_9+\lvert z\rangle_{11}-\lvert z\rangle_{13}-\lvert y\rangle_{14}-\lvert y\rangle_{15}+\lvert y\rangle_{16}$
	4	$\lvert z\rangle_5+\lvert y\rangle_7-\lvert y\rangle_9-\lvert y\rangle_{11}+\lvert y\rangle_{13}-\lvert z\rangle_{14}+\lvert z\rangle_{15}-\lvert z\rangle_{16}$
y	1	$\lvert s\rangle_5+\lvert s\rangle_6+\lvert s\rangle_8-\lvert s\rangle_{10}-\lvert s\rangle_{12}-\lvert s\rangle_{14}+\lvert s\rangle_{15}-\lvert s\rangle_{16}$
	2	$\lvert y\rangle_5+\lvert y\rangle_6+\lvert y\rangle_8+\lvert y\rangle_{10}+\lvert y\rangle_{12}+\lvert y\rangle_{14}+\lvert y\rangle_{15}+\lvert y\rangle_{16}$
	3	$\lvert x\rangle_5+\lvert z\rangle_6-\lvert z\rangle_8-\lvert z\rangle_{10}+\lvert z\rangle_{12}-\lvert x\rangle_{14}-\lvert x\rangle_{15}+\lvert x\rangle_{16}$
	4	$\lvert z\rangle_5+\lvert x\rangle_6-\lvert x\rangle_8+\lvert x\rangle_{10}-\lvert x\rangle_{12}+\lvert z\rangle_{14}-\lvert z\rangle_{15}-\lvert z\rangle_{16}$
z	1	$\lvert s\rangle_6+\lvert s\rangle_7-\lvert s\rangle_8-\lvert s\rangle_9+\lvert s\rangle_{10}-\lvert s\rangle_{11}-\lvert s\rangle_{12}+\lvert s\rangle_{13}$
	2	$\lvert z\rangle_6+\lvert z\rangle_7+\lvert z\rangle_8+\lvert z\rangle_9+\lvert z\rangle_{10}+\lvert z\rangle_{11}+\lvert z\rangle_{12}+\lvert z\rangle_{13}$
	3	$\lvert y\rangle_6+\lvert x\rangle_7-\lvert y\rangle_8-\lvert x\rangle_9-\lvert y\rangle_{10}+\lvert x\rangle_{11}+\lvert y\rangle_{12}-\lvert x\rangle_{13}$
	4	$\lvert x\rangle_6+\lvert y\rangle_7+\lvert x\rangle_8+\lvert y\rangle_9-\lvert x\rangle_{10}-\lvert y\rangle_{11}-\lvert x\rangle_{12}-\lvert y\rangle_{13}$
θ	5	$2\lvert s\rangle_5-\lvert s\rangle_6-\lvert s\rangle_7-\lvert s\rangle_8-\lvert s\rangle_9-\lvert s\rangle_{10}-\lvert s\rangle_{11}-\lvert s\rangle_{12}$ $-\lvert s\rangle_{13}+2\lvert s\rangle_{14}+2\lvert s\rangle_{15}+2\lvert s\rangle_{16}$
	6	$2\lvert x+y\rangle_5-\lvert y+z\rangle_6-\lvert x+z\rangle_7+\lvert -y+z\rangle_8$ $+\lvert -x+z\rangle_9+\lvert y-z\rangle_{10}+\lvert x+z\rangle_{11}+\lvert y+z\rangle_{12}$ $+\lvert x-z\rangle_{13}+2\lvert x-y\rangle_{14}+2\lvert -x+y\rangle_{15}-2\lvert x+y\rangle_{16}$
	7	$2\lvert z\rangle_5-\lvert x\rangle_6-\lvert y\rangle_7+\lvert x\rangle_8+\lvert y\rangle_9+\lvert x\rangle_{10}-\lvert y\rangle_{11}-\lvert x\rangle_{12}$ $+\lvert y\rangle_{13}-2\lvert z\rangle_{14}-2\lvert z\rangle_{15}+2\lvert z\rangle_{16}$
ϵ	5	$\lvert s\rangle_6-\lvert s\rangle_7+\lvert s\rangle_8-\lvert s\rangle_9+\lvert s\rangle_{10}-\lvert s\rangle_{11}+\lvert s\rangle_{12}-\lvert s\rangle_{13}$
	6	$\lvert y+z\rangle_6+\lvert -x-z\rangle_7+\lvert y-z\rangle_8+\lvert -x+z\rangle_9$ $+\lvert -y+z\rangle_{10}+\lvert x+z\rangle_{11}-\lvert y+z\rangle_{12}+\lvert x-z\rangle_{13}$
	7	$\lvert x\rangle_6-\lvert y\rangle_7-\lvert x\rangle_8+\lvert y\rangle_9-\lvert x\rangle_{10}-\lvert y\rangle_{11}+\lvert x\rangle_{12}+\lvert y\rangle_{13}$

TABLE XI. Relation between the site indices and the site positions of the atomic spheres that are occupied with atoms. The site indices are used in Tables VIII–X. Note that three distinct trigonal shells are included, each of which correspond to the site indices 1–4.

Site indices	Sites
0	(0,0,0)
1–4	$(1,1,1)$, $(\bar{1},1,\bar{1})$, $(1,\bar{1},\bar{1})$, $(\bar{1},1,1)$
1–4	$(2,2,2)$, $(\bar{2},2,2)$, $(2,\bar{2},2)$, $(2,2,\bar{2})$
1–4	$(2,2,\bar{2})$, $(\bar{2},2,2)$, $(2,\bar{2},2)$, $(2,2,\bar{2})$
5–16	$(1,1,\bar{3})$, $(\bar{3},1,1)$, $(1,\bar{3},1)$, $(3,1,\bar{1})$, $(1,\bar{3},\bar{1})$, $(\bar{3},1,\bar{1})$, $(1,3,1)$, $(3,1,1)$, $(1,3,1)$, $(1,1,3)$, $(\bar{1},1,3)$, $(1,\bar{1},3)$
17–22	$(2,0,0)$, $(0,2,0)$, $(0,0,2)$, $(0,0,\bar{2})$, $(0,\bar{2},0)$, $(\bar{2},0,0)$

$$\langle r^{-3}\rangle_l^j=\int_0^{s_{R_j}}\frac{1}{r^3}|\varphi_{R_jl}(r)|^2r^2dr,\quad l=p,d, \tag{A5a}$$

$$P_l^j=\frac{\mu_0}{4\pi}g_N^j\mu_N\mu_B\langle r^{-3}\rangle_l^j,\quad l=p,d, \tag{A5b}$$

$$A_d^j=\frac{\mu_0}{4\pi}g_N^j\mu_N\mu_B\frac{1}{R_j^3}, \tag{A5c}$$

$$A_{c,\alpha}^j=\tfrac{2}{3}\,\mu_0g_N^j\mu_N\mu_B|\Psi_\alpha^j(0)|^2,\quad \alpha=t_2,e, \tag{A5d}$$

where s_{R_j} is the radius of the atomic sphere centered around the site R_j and $|\Psi_\alpha^j(0)|^2$ has to be taken from Table XII.

Using the parameters (25) our results will be summarized with the notation

$$A_{ik}^j=a_{ik}^{\mathrm{CP},j}+a_{ik}^{c,j}+a_{ik}^{l,j}+a_{ik}^{d,j},$$

where the superscripts CP, c, l, and d refer to the contribution from the core polarization, from the Fermi contact interaction, from the orbital angular momentum, and from the dipole-dipole interaction listed in (12), respectively. We obtain the following results.

1. hfi with the iron nucleus

$$A_{ik}^{\mathrm{Fe}}=0\,\forall\, i\neq k,$$

$$A_{ii}^{\mathrm{Fe}}=a_l+a_d+a_{\mathrm{CP}},\quad i=x,y,z,$$

$$a_l=\tfrac{4}{3}\,\beta_0^2P_d^{\mathrm{Fe}}, \tag{A6}$$

$$a_d=-\tfrac{2}{63}\,g_s\beta_0^2P_d^{\mathrm{Fe}},$$

$$a_{\mathrm{CP}}=\tfrac{5}{6}\,A_{\mathrm{CP}}^{\mathrm{Fe}}.$$

2. Trigonal shells

$$a_{xy}^{\eta,j}=a_{yx}^{\eta,j}=\pm a_{xz}^{\eta,j}=\pm a_{zx}^{\eta,j}=\pm a_{yz}^{\eta,j}=\pm a_{zy}^{\eta,j},$$

$$\eta=\mathrm{CP},c,l,d,$$

$$a_{xx}^{\eta,j}=a_{yy}^{\eta,j}=a_{zz}^{\eta,j},\quad \eta=\mathrm{CP},c,l,d,$$

$$a_{xx}^{\mathrm{CP},j}=\tfrac{5}{3}\,A_{\mathrm{CP}}^j,$$

$$a_{xy}^{\mathrm{CP},j}=0,$$

$$a_{xx}^{c,j}=\frac{5}{18}\,\frac{g_s}{2}A_{c,t_2}^j,$$

$$a_{xy}^{c,j}=-\frac{1}{18}\,\frac{g_s}{2}A_{c,t_2}^j, \tag{A7}$$

$$a_{xx}^{l,j}=-\tfrac{1}{3}\,(\beta_2^2-\tfrac{1}{2}\,\beta_3^2)P_p^j,$$

$$a_{xy}^{l,j}=\tfrac{2}{3}\left(-\tfrac{1}{4}\,\beta_3^2+\frac{1}{\sqrt{8}}\beta_2\beta_3\right)P_p^j,$$

$$a_{xx}^{d,j}=-\frac{g_s}{18}[\beta_2^2+\tfrac{1}{10}\,\beta_3^2-\beta_4^2]P_p^j,$$

TABLE XII. Contact densities $|\Psi_\alpha^j(0)|^2$ for the silicon ligand shells for different irreducible representations used in Eq. (A5d).

	Shell		
α	Trigonal	Rhombic	Monoclinic
t_2	$\beta_1^2\|\varphi_{R_j0}(0)\|^2$	$\gamma_1^2\|\varphi_{R_j0}(0)\|^2$	$\delta_1^2\|\varphi_{R_j0}(0)\|^2$
e	–	$\gamma_3^2\|\varphi_{R_j0}(0)\|^2$	$\delta_5^2\|\varphi_{R_j0}(0)\|^2$

TABLE XIII. Data for the products of the prefactors $\beta_i\beta_k$, $\gamma_i\gamma_k$, and $\delta_i\delta_k$ (times 10^{-4}) defined in the linear combinations (21) for Si:Fe_i^+. The data are determined from our self-consistently calculated magnetization densities Eq. (17). The products listed are used in Eqs. (A6)–(A9). For brevity we list the combinations of indices i,j only.

	i,k								
Site	2,2	2,3	2,4	3,3	3,4	4,4	6,6	6,7	7,7
Si(1,1,1)	218	−285		−141		681			
Si(2,2,2)	236	270		207		6.14			
Si(2,2,$\bar{2}$)	−9.83	4.18		−3.53		5.59			
Si(2,0,0)	23.6					103			
Si(1,1,$\bar{3}$)	−23.3	35.5	20.2	−54.8	31.2	−17.5	171	−154	129
Fe(0,0,0)		$\beta_0^2=8288$			$\beta_{00}^2=7156$				

$$a_{xy}^{d,j}=\frac{g_s}{2}\left(\frac{1}{5}\frac{1}{\sqrt{8}}\beta_2\beta_3+\tfrac{1}{18}\tfrac{1}{5}\tfrac{11}{2}\beta_3^2-\tfrac{1}{9}\beta_4^2\right)P_p^j$$
$$+\tfrac{5}{9}(\beta_0^2+2\beta_{00}^2)g_sA_d^j.$$

3. Rhombic shells

$$a_{ik}^{\eta,j}=0\,\forall\, i\neq k,\quad \eta=\mathrm{CP},c,l,d,$$
$$a_{yy}^{\eta,j}=a_{zz}^{\eta,j},\quad \eta=\mathrm{CP},c,l,d,$$
$$a_{xx}^{\mathrm{CP},j}=a_{yy}^{\mathrm{CP},j}=\tfrac{5}{3}A_{\mathrm{CP}}^j,$$
$$a_{xx}^{c,j}=(\tfrac{1}{18}A_{c,t_2}^j+\tfrac{5}{27}A_{c,e}^j)g_s,$$
$$a_{yy}^{c,j}=(\tfrac{1}{9}A_{c,t_2}^j+\tfrac{5}{27}A_{c,e}^j)g_s,$$
$$a_{kk}^{l,j}=0,\quad k=x,j,z,$$
$$a_{xx}^{d,j}=\tfrac{1}{9}(\tfrac{2}{5}\gamma_2^2+\tfrac{4}{3}\gamma_4^2)g_sP_p^j \qquad \text{(A8)}$$
$$+\tfrac{5}{9}g_s(\beta_0^2+2\beta_{00}^2)\frac{3(-R_j)_x^2-R_j^2}{R_j^2}A_d^j,$$
$$a_{yy}^{d,j}=-\tfrac{2}{45}(\gamma_2^2+\tfrac{5}{3}\gamma_4^2)g_sP_p^j+\tfrac{5}{9}g_s(\beta_0^2+2\beta_{00}^2)$$
$$\times\frac{3(-R_j)_x^2-R_j^2}{R_j^2}A_d^j.$$

4. Monoclinic shells

$$a_{kk}^{\mathrm{CP},j}=\tfrac{5}{3}A_{\mathrm{CP}}^j,\quad k=x,y,z,$$
$$a_{ik}^{\mathrm{CP},j}=0\,\forall\, i\neq k,$$
$$a_{kk}^{c,j}=\tfrac{5}{9}g_s(\tfrac{1}{8}A_{c,t_2}^j+\tfrac{1}{12}A_{c,e}^j),\quad k=x,y,z,$$
$$a_{ik}^{c,j}=\tfrac{1}{9}g_s\tfrac{1}{8}A_{c,t_2}\,\forall\, i\neq k,$$
$$a_{xx}^{l,j}=-\tfrac{1}{6}(\delta_2^2-\delta_3\delta_4)P_p^j,$$
$$a_{xy}^{l,j}=a_{zy}^{l,j}=\tfrac{1}{6}(\delta_2\delta_3-\delta_3\delta_4)P_p^j,$$
$$a_{xz}^{l,j}=a_{yz}^{l,j}=\tfrac{1}{6}(\delta_2\delta_4-\delta_3\delta_4)P_p^j,$$
$$a_{yx}^{l,j}=\tfrac{1}{6}(\delta_2\delta_3-\delta_4^2)P_p^j,$$
$$a_{yy}^{l,j}=-\tfrac{1}{6}(\delta_2^2-\delta_4^2)P_p^j,$$
$$a_{zx}^{l,j}=-\tfrac{1}{6}(\delta_3^2-\delta_2\delta_4)P_p^j,$$
$$a_{zz}^{l,j}=-\tfrac{1}{6}(\delta_2^2-\delta_3^2)P_p^j,$$

TABLE XIV. Hyperfine parameter (in MHz) determined from the self-consistently calculated magnetization density for Si:Fe_i^+ [see Eqs. (12b) and (A5)].

j	A_{CP}^j	A_{c,t_2}^j	$A_{c,e}^j$	P_p^j	A_d^j
Si(1,1,1)	−0.417	−6.752		−275.55	−0.604
Si(2,2,2)	−1.660	7.197		−272.37	−0.604
Si(2,2,$\bar{2}$)	−0.007	0.629		−272.28	−0.604
Si(2,0,0)	4.433	0.121	1.606	−273.01	−0.393
Si(1,1,$\bar{3}$)	−1.912	4.442	−25.43	−272.39	−0.086
Fe(0,0,0)	−12.41			$P_d=43.52$	

$$a_{xx}^{d,j}=-\frac{1}{36}\frac{g_s}{10}(10\delta_2^2+\delta_3^2+\delta_4^2-\tfrac{10}{3}\delta_6^2+\tfrac{20}{3}\delta_7^2)P_p^j + \tfrac{5}{9}g_s(\beta_0^2+2\beta_{00}^2)\frac{3(-R_j)_x^2-R_j^2}{R^2}A_d^j, \quad \text{(A9)}$$

$$a_{xy}^{d,j}=\frac{1}{36}\frac{g_s}{10}(13\delta_2\delta_3-\delta_4^2+12\delta_3\delta_4+10\delta_6^2)P_p^j + \tfrac{5}{9}g_s(\beta_0^2+2\beta_{00}^2)\frac{3(-R_j)_x(-R_j)_y}{R_j^2}A_d^j,$$

$$a_{xz}^{d,j}=\frac{1}{36}\frac{g_s}{10}(14\delta_2\delta_4+12\delta_3\delta_4+10\sqrt{2}\,\delta_6\delta_7-\tfrac{1}{2}\delta_3^2)P_p^j + \tfrac{5}{9}g_s(\beta_0^2+2\beta_{00}^2)\frac{3(-R_j)_x(-R_j)_z}{R_j^2}A_d^j,$$

$$a_{yx}^{d,j}=\frac{1}{36}\frac{g_s}{10}(13\delta_2\delta_3+2\delta_4^2+9\delta_3\delta_4+10\delta_6^2)P_p^j + \tfrac{5}{9}g_s(\beta_0^2+2\beta_{00}^2)\frac{3(-R_j)-x(-R_j)_y}{R_j^2}A_d^j,$$

$$a_{yy}^{d,j}=-\frac{1}{36}\frac{g_s}{10}(10\delta_2^2-11\delta_3^2+10\delta_4^2+3\delta_3\delta_4-\tfrac{10}{3}\delta_6^2 + \tfrac{20}{3}\delta_7^2)P_p^j+\tfrac{5}{9}g_s(\beta_0^2+2\beta_{00}^2)\frac{3(-R_j)_y^2-R_j^2}{R_j^2}A_d^j,$$

$$a_{yz}^{d,j}=\frac{1}{36}\frac{g_s}{10}(-\delta_2\delta_3+11\delta_3\delta_4+14\delta_2\delta_4 + 10\sqrt{2}\,\delta_6\delta_7)P_p^j\tfrac{5}{9}g_s(\beta_0^2+2\beta_{00}^2)\frac{(-R_j)_y(-R_j)_z}{R_j^2}A_d^j,$$

$$a_{zx}^{d,j}=\frac{1}{36}\frac{g_s}{10}(13\delta_2\delta_4+9\delta_3\delta_4+10\sqrt{2}\,\delta_6\delta_7+2\delta_3^2)P_p^j + \tfrac{5}{9}g_s(\beta_0^2+2\beta_{00}^2)\frac{3(-R_j)_x(-R_j)_z}{R_j^2}A_d^j,$$

$$a_{zy}^{d,j}=\frac{1}{36}\frac{g_s}{10}(11\delta_3\delta_4-\delta_2\delta_4+14\delta_2\delta_3+10\sqrt{2}\,\delta_6\delta_7)P_p^j + \tfrac{5}{9}g_s(\beta_0^2+2\beta_{00}^2)\frac{3(-R_j)_y(-R_j)_z}{R_j^2}A_d^j,$$

$$a_{zz}^{d,j}=-\frac{1}{36}\frac{g_s}{10}(10\delta_2^2+10\delta_3^2-11\delta_4^2+3\delta_3\delta_4+\tfrac{20}{3}\delta_6^2 - \tfrac{40}{3}\delta_7^2)P_p^j+\tfrac{5}{9}g_s(\beta_0^2+2\beta_{00}^2)\frac{3(-R_j)_z^2-R_j^2}{R_j^2}A_d^j.$$

In order to calculate data for the hfi with the iron nucleus and with several silicon nuclei we use the calculated magnetization density as indicated in Eq. (17) to calculate the prefactors and the hfi parameters defined in Eq. (A5) and Eq. (12b). Tables XIII and XIV show the corresponding data for six positions of nuclear spins. Using these data together with Eqs. (A6)–(A9) we get the results summarized in Table V.

[1] G.W. Ludwig and H.H. Woodbury, in *Solid State Physics: Advances in Research and Applications*, edited by H. Ehrenreich, F. Seitz, and D. Turnbull (Academic Press, New York, 1962), Vol. 13, p. 223.

[2] E. Weber and H.G. Riotte, J. Appl. Phys. **51**, 1484 (1980).

[3] H. Lemke, Phys. Status Solidi A **64**, 215 (1981).

[4] K. Wünstel and P. Wagner, Solid State Commun. **40**, 797 (1981).

[5] W. Gehlhoff and K.H. Segsa, Phys. Status Solidi A **41**, K21 (1977).

[6] E.G. Sieverts, S.H. Muller, C.A.J. Ammerlaan, and E.R. Weber, Solid State Commun. **47**, 631 (1983).

[7] S. Greulich-Weber, J.R. Niklas, E.R. Weber, and J.-M. Spaeth, Phys. Rev. B **30**, 6292 (1986).

[8] D.A. van Wezep, T. Gregorkiewicz, E.G. Sieverts, and C.A.J. Ammerlaan, Phys. Rev. B **34**, 4511 (1986).

[9] E.G. Sieverts, D.A. van Wezep, R. van Kemp, and C.A.J. Ammerlaan, in Defects in Semiconductors, edited by H. von Bardeleben [Mater. Sci. Forum. **10–12**, 729 (1986)].

[10] J.J. van Kooten, E.G. Sieverts, and C.A.J. Ammerlaan, Phys. Rev. B **37**, 8949 (1988).

[11] J. Kübler, A.E. Kumm, H. Overhof, P. Schwalbach, M. Hartick, E. Kankeleit, B. Keck, L. Wende, and R. Sielemann, Z. Phys. B **92**, 155 (1993).

[12] C.A.J. Ammerlaan, Solid State Phenom. **6 & 7**, 591 (1989).

[13] G.G. DeLeo, G.D. Watkins, and W.B. Fowler, Phys. Rev. B **23**, 1851 (1981); **25**, 4962 (1982); **25**, 4972 (1982).

[14] P. Hohenberg and W. Kohn, Phys. Rev. **136**, B864 (1964).

[15] W. Kohn and L.J. Sham, Phys. Rev. **140**, A1133 (1965).

[16] U. von Barth and L. Hedin, J. Phys. C **5**, 1629 (1972).

[17] D. Ceperley, Phys. Rev. B **18**, 3126 (1978).

[18] D.M. Ceperley and B.J. Alder, Phys. Rev. Lett. **45**, 566 (1980).

[19] A. Zunger and U. Lindefelt, Phys. Rev. B **26**, 5989 (1982); **27**, 1191 (1983).

[20] O. Gunnarsson, O. Jepsen, and O.K. Andersen, Phys. Rev. B **27**, 7144 (1983).

[21] A. Zunger, Phys. Rev. B **28**, 3628 (1983); in *Solid State Physics: Advances in Research and Applications*, edited by F. Seitz and D. Turnbull (Academic, New York, 1986), Vol. 39, p. 276.

[22] A. Fazzio, M.J. Caldas, and A. Zunger, Phys. Rev. B **30**, 3430 (1984).

[23] H. Katayama-Yoshida and A. Zunger, Phys. Rev. Lett. **53**, 1256 (1984); Phys. Rev. B **31**, 7877 (1985); **31**, 8317 (1985).

[24] U. Lindefelt, Phys. Rev. B **28**, 4510 (1983).

[25] U. Lindefelt and A. Zunger, Phys. Rev. B **30**, 1102 (1984).

[26] F. Beeler, O.K. Andersen, and M. Scheffler, Phys. Rev. Lett. **55**, 1498 (1985); Phys. Rev. B **41**, 1603 (1990).

[27] F. Beeler, Ph.D. thesis, Universität Stuttgart, 1986.
[28] H. Katayama-Yoshida and N. Hamada, Phys. Rev. B **35**, 401 (1987).
[29] F. Beeler and M. Scheffler, Mater. Sci. Forum **38-41**, 257 (1989).
[30] F.S. Ham, Phys. Rev. **138**, A1727 (1965).
[31] A. Thilderkvist, G. Grossmann, M. Kleverman, and H.G. Grimmeiss, in *Impurities, Defects and Diffusion in Semiconductors: Bulk and Layered Structures*, edited by D. J. Wolford, J. Bernholc, and E. E. Haller, MRS Symposia Proceedings No. 163 (Materials Research Society, Pittsburgh, 1990), p. 51.
[32] A. Thilderkvist, M. Kleverman, G. Grossmann, and H.G. Grimmeiss, in *The Physics of Semiconductors*, edited by E. N. Anastassakis and J. D. Joannopoulos (World Scientific, Singapore, 1990), p. 895.
[33] A. Thilderkvist, G. Grossmann, M. Kleverman, and H.G. Grimmeiss, Mater. Sci. Forum **143-147**, 165 (1994).
[34] J. C. Slater, in *Theory of Molecules and Solids, Vol. I, Electronic Structure of Molecules* (McGraw-Hill Book Company, New York, 1963), App. 12.
[35] The $E_{\nu l}$ are chosen to be the center of gravity of the band gap and of the valence bands for the two integration paths around the gap and around the valence bands, respectively.
[36] We exploit that the $f^{\alpha}_{\kappa\mu,\overline{Rl}}(E,\vec{r})$ are real functions for the point groups T_d, C_{3v}, and C_{2v}.
[37] J. Owen and J.H.M. Thornley, Rep. Prog. Phys. **29**, 676 (1966).
[38] C.O. Rodriguez, S. Brand, and M. Jaros, J. Phys. C **13**, L333 (1980).
[39] J.S. Griffith, *The Theory of Transition-Metal Ions* (Cambridge University Press, Cambridge, England, 1971).
[40] S. Sugano, Y. Tanabe, and H. Kamimura, *Multiplets of the Transition-Metal Ions in Crystals* (Academic Press, New York, 1970).
[41] H. Weihrich, Ph.D. thesis, Universität Paderborn, 1995 (unpublished).
[42] A. Abragam, J. Horowitz, and M.H.L. Pryce, Proc. R. Soc. London, Ser. A **230**, 169 (1955).
[43] See, e.g., A. Abragam and B. Bleaney, *Electron Paramagnetic Resonance Of Transition Ions* (Dover, New York, 1970), Chap. 17.6.
[44] S. Blügel, H. Akai, R. Zeller, and P.H. Dederichs, Phys. Rev. B **35**, 3271 (1987).
[45] See, e.g., H. Overhof, in *Hyperfine Interaction of Defects in Semiconductors*, edited by G. Langouche (Elsevier, Amsterdam, 1992), Chap. 9.
[46] H. Weihrich, Diploma thesis, Universität Paderborn, 1991 (unpublished).
[47] P. Pathikrit and B.A. Bunker, Bull. Am. Phys. Soc. **30**, 276 (1985).
[48] J. Olajos, B. Bech Nielsen, M. Kleverman, P. Omling, P. Emanuelsson, and H.G. Grimmeiss, Appl. Phys. Lett. **53**, 2507 (1988).
[49] For the notation of our many-particle wave functions we refer to S. Sugano, Y. Tanabe, and H. Kamimura, *Multiplets of the Transition-Metal Ions in Crystals* (Ref. 40).
[50] We use overstriked symbols to indicate many-particle eigenfunctions of the fictitious angular momentum $\tilde{l}=1$, and we use the tilde to indicate one-particle eigenfunctions of the fictitious angular momentum $\tilde{l}=1$.
[51] The three holes of the t_2e^2 hole configuration have the same magnetization density as the seven electrons of the complementary $t_2^5e^2$ configuration.
[52] This is the reason why some of the ''squared'' prefactors are negative (see Table XIII).
[53] H. Weihrich and H. Overhof (unpublished).
[54] P. Alteheld, S. Greulich-Weber, J.-M. Spaeth, H. Weihrich, H. Overhof, and M. Höhne, Phys. Rev. B **45**, 4998 (1995).
[55] H. Weihrich, H. Overhof, P. Alteheld, S. Greulich-Weber, and J.-M. Spaeth, Phys. Rev. B **45**, 5007 (1995).
[56] This is, of course, no surprise, because the important symmetry constraints for a hfi matrix do not originate from the full symmetry of the defect but rather from that subgroup of the point group of the defect which leaves invariant the positions both of the impurity atom and also of the ligand nucleus in question.
[57] Note that we use the same symbols f^{α}_{k}, g^{α}_{k}, and h^{α}_{k} in Tables VII–X for the unnormalized linear combinations.
[58] Here we exploit the fact that the defect orbitals are strongly localized around the iron site.